High-Frequency Acoustic Propagation in a Bottom Boundary Layer: The Acoustic Medium Stability Experiment

G. Minot Clements
Dynamics Technology, Inc.
1555 Wilson Blvd., Suite 320
Arlington, VA 22209

Abstract

The Acoustic Medium Stability Experiment used a horizontal array of hydrophones to measure high-frequency acoustic propagation in a coastal shelf environment. Medium properties varied along the acoustic path, which slanted through a vertically inhomogeneous bottom boundary layer. We apply synthetic spatial aperture filtering to isolate the contribution to acoustic scintillation from medium fluctuations localized at a fixed altitude above the bottom. Using Rytov theory, we compare the filtered acoustic data with direct measurements of medium fluctuations obtained at a corresponding altitude. Analyzing several different examples, we find good agreement between acoustic and temperature-conductivity sensor measurements using a simple, anisotropic model for the three-dimensional spectrum of medium fluctuations.

1. Introduction

Successful formation of an image with a synthetic aperture sonar (SAS) requires that the acoustic signal be phase coherent over the interval when a given point in the scene is ensonified by the transmitter (or is visible to the receiver). In 1992 an experiment was conducted to measure medium-induced acoustic phase fluctuations at high frequencies (≥100 kHz) in a coastal shelf environment. The experiment, known as AMSE (for Acoustic Medium Stability Experiment), was intended to characterize the potential degradation of SAS performance by acoustic medium fluctuations in an environment of interest for SAS operation.

Compared with previous SAS feasibility experiments (Tardif, 1973; Christoff et al., 1982; Gough and Hayes, 1989), AMSE operated at higher frequencies and/or pathlengths, and consequently observed larger phase fluctuations. The AMSE also deployed an array of acoustic receivers and included collection of simultaneous sea-truth data near the acoustic path, making it possible to identify some of the phenomenology associated with acoustic fluctuations. In these respects the AMSE is more closely comparable to a recent series of acoustical oceanography experiments carried out in a similar frequency regime (Farmer et al., 1987; Farmer and Crawford, 1991; Farmer and DiIorio, 1992). However, the AMSE differs from these experiments in two important respects. It was located in a coastal shelf environment, while the cited experiments were located in a narrow tidal channel or bay. Also, the AMSE used a larger acoustic receiver array (10 horizontally spaced elements rather than 2 or 4). In view of these differences, it is interesting to apply some of the spatial filtering methods explored in these papers to the AMSE data.

Spatial filtering uses space and time diversity in the acoustic signal to sound medium properties (such as flow speed or turbulence intensity) along the propagation path. Originally worked out for optical and microwave propagation in the atmosphere, it has also been applied to ocean acoustics (Crawford et al., 1990; Farmer and Clifford, 1986). The classic method for sounding assumes an array of receivers and either an array of sources or a moving source. A procedure closely related to tomography is used to retrieve medium properties along the propagation path. The method investigated in this paper is synthetic spatial aperture filtering (Farmer and Crawford, op. cit.), which relies on advection of frozen refractive index structure (Taylor's hypothesis) by a moving medium to "synthesize" spatially diverse sources, and on weak (Rytov) scattering theory to interpret the results.

An unique feature of the AMSE, motivated by SAS geometries, was the altitude difference between the acoustic projector and the receiver array. Because of this altitude difference, the acoustic path traversed much of the bottom boundary layer. Thus medium property variations in the vertical were encountered by the acoustic signal at different positions along the acoustic path. This raises the interesting possibility of sounding the boundary layer in the vertical by using spatial filtering to focus the array at different path positions. Because AMSE only made use of a single acoustic transmitter and had a limited suite of environmental sensors, a full investigation of this concept with the AMSE

data was not possible. A more limited test of the concept, comparing medium properties inferred from the acoustic signal with medium property measurements at a single altitude, was possible and is the subject of this paper.

2. Description of the Experiment

The AMSE was conducted during October, 1992 in coastal waters off of Ft. Lauderdale, Florida. The test site was 5.5 km offshore, on the bottom in 175 m of water. Bottom composition is hard sand, with smooth topography sloping off to the east (1-2° inclination).

Mean currents in the test area are quite variable. The site is near the western border of the Florida current, in a zone where currents are formed by a variety of factors, including the dominant and varying effects of the Florida current, local tidal currents, weather-induced surface currents, and coastal counter-currents. Weather conditions during the experiment varied from calm to several days of 30-40 knot winds generated by a tropical depression. A correspondingly large range of mean currents (from quiescent to 40 cm/s) was observed at the bottom.

10 hydrophone receivers were deployed horizontally on a 33 m wide rigid truss structure situated 22.5 m above the sea floor (Figure 1). Inter-hydrophone spacings were chosen to provide a low-redundancy selection of spatial lags; 21 different spacings ranging from 0.5 m to 33 m are present in the array. The hydrophone array was aligned parallel with the prevailing current (NNE) in order to minimize flow disturbance by the structure.

Interior to the pipe carrying the hydrophones, a distributed motion sensor comprised of laser targets mounted to the pipe wall and a laser source mounted at the pipe support allowed continuous monitoring of structural deflections which might otherwise be interpreted as acoustic phase fluctuations. Analysis of motion sensor data shows that structural deflections were always very small, translating to phase contributions well below the limiting accuracy imposed by acoustic receiver electronics on phase estimation.

The experiment geometry is depicted in figure 2. The acoustic projector was a 10.5 cm diameter hemispherical source, designed with sufficient beamwidth to illuminate the receiver array within 1 dB of peak power. This projector was mounted on a rigid tripod standing 3 m above the bottom. The projector assembly was deployed at 300 m range from the receive array on the offshore (east) side. Triangulation using time of flight measurements after deployment indicated that the projector azimuth relative to array broadside was -8.8°.

Data were collected at frequencies of 100 kHz, 143 kHz, 180 kHz, 253 kHz, and 300 kHz. Pulses of 750 or 1500 μs duration (75 or more acoustic cycles depending on frequency) were transmitted at 2 s intervals. Received pulses were mixed down to 25 kHz IF and sampled at 83.3 kHz with 12-bit A/D converters. The 0.5 m path length difference between the direct and bottom reflection paths was ample to allow phase

estimation from the clean cycles at the leading edge of the received pulse. Predicted rms phase estimation error ranged from 1.2° at 20 dB SNR to 3.8° at 10 dB SNR to 12° at 0 dB SNR.

Achieved SNRs were often below design specification for the higher frequencies. Combined with amplitude scintillation, this caused errors in phase tracking resulting in noisy phase histories. Almost half of the phase runs were rendered unusable by phase tracking errors. A probable contributing factor to the low SNR was the error in positioning the projector. Receiver #10, which was furthest outboard from the actual projector position, was more susceptible to phase tracking problems than the other receivers.

Four conductivity-temperature (CT) sensors (Ocean Sensors OS100) were mounted on the receiver truss structure at elevations of 6.1 m, 11.9 m, 17.4 m, and 22.9 m above the sea floor. A horizontal current meter (Marsh-McBirney 500 series electromagnetic) was mounted near the CT at 11.9 m. The CT's and current meter were mounted several beam diameters away from the nearest structural element to avoid potential flow and wake effects. Data from all instruments were sampled at 20 Hz.

In order to characterize vertical ocean structure, a boat equipped with a profiling CTD was stationed near the acoustic test site at periods during the acoustic data collection. The CTD was raised and lowered over the lowermost 30 meters in order to collect data over the same aperture as the acoustic beam path. Unfortunately, because of winds and currents and a lack of accurate navigational equipment on the boat, its position drifted rapidly over the course of a run. Subsequent analysis showed that most profiles were collected substantially inshore from the experiment site and consequently did not usefully characterize the vertical structure in the acoustic propagation path.

More than 50 hours of acoustic and sea-truth data was collected over the experiment. A total of 655 minutes of this data was calibrated for analysis. A brief summary of this data is presented in the following table:

Date (1992)	Run numbers	Data collected (minutes)	Acoustic data frequencies collected (kHz)	Current speed range (cm/s)	Vertical ΔT range (C)
10/15	1-3,8-10	76	100, 253	2-12	1.2-2.5
10/16	11-14	73	100, 253	10-25	1.5-2
10/17	15-25	140	100, 253	25-35	5.5-7
10/21	4-5	48	100, 180, 253	15-40	1.5-3
10/26	6-7,26-35	175	100, 180, 253, 300	21-30	1-3.5
10/27	36-45	143	100, 180, 253, 300	3-17	1.5-7.5

Here vertical ΔT refers to the temperature difference measured between the sensors on the top and bottom of the receiver truss structure. For a shelf bottom site this data set contains a good variety of environmental conditions, ranging from slack, highly stratified water (10/27) to 40 cm/s, well-mixed water (10/21).

3. Acoustic and Environmental Data

Figure 3a shows 1-minute averaged temperature and salinity data from the array sensors for runs on 10/17. The CT sensors, labeled CT3, CT2, CT1, and CT4 in order of altitude, were at 6.1 m, 11.9 m, 17.4 m, and 22.9 m above the bottom, respectively. The stable temperature stratification and unstable salinity stratification observed in these data were typical of the runs analyzed. Figure 3b shows the squared buoyancy frequency (in units of radian/s) and density ratio R_ρ derived from the same data. Because of the large differencing interval (~5.5 m) these values are only qualitative indications of the true values. For this group of runs, it is reasonable to assume that the stratification supported internal waves with Brunt-Vaisala frequency in the range 10-20 cph and that density ratios occurred that were suitable for rapid growth of salt fingers (Schmitt, 1979).

Figure 4a shows 100 kHz acoustic phase data for the ten receivers during run 37. Such large synchronous phase drifts (where all receivers track), of 10000° (30 cycles) or more over 15 minutes, were not uncommon in the AMSE data. As an example, such phase drifting could be produced by a temperature change of O(0.5 °C) over 15 minutes affecting most of the acoustic path. Temperature changes of this magnitude were observed on these time scales. However, attempts to correlate phase variations directly with observed temperature and salinity fluctuations were not successful. This suggests that horizontal correlation scales associated with the medium structure were less than the O(150 m) average separation between the CT sensors on the array structure and the acoustic path.

Figures 4b and 4c show phase and log-amplitude variations for run 37 on a shorter time scale. Phase rates of up to 50°/second are evident, with substantial but not perfect coherence between different receivers for both phase and amplitude. The repetition of identifiable temporal structures in the acoustic signal at different array elements and the agreement of their speed across the array with the scaled current speed is evidence that the medium fluctuations satisfy Taylor's hypothesis over the time scales of interest.

4. Space-Time Filtering

Theory

In the unsaturated (weak fluctuation) regime, the spatial power spectrum of sound speed structure is related to covariances of the phase (ϕ) and log-amplitude (χ) by (Lee and Harp, 1969)

$$B_{\substack{\chi \\ \varphi}}(\Delta\underline{r},\Delta t) \approx 2\pi k_i^2 L \int_0^1 d\eta \int d^2k e^{i\underline{k}\cdot\Delta\underline{r}\eta - i\underline{k}\cdot\underline{v}(\eta)\Delta t} H_{\substack{\chi \\ \varphi}}(\underline{k};\eta) F_n(\underline{k};\eta) \qquad (1)$$

where k_i denotes acoustic wavenumber and L is the pathlength. Here F_n is the three-dimensional spatial power spectrum of refractive index fluctuation, evaluated at transverse wavenumbers $\underline{k}$. F_n also depends on the scaled path parameter η=x/L, reflecting an assumption that the refractive index structure is locally stationary. H denotes the usual filter function for spherical wave propagation

$$H_{\underset{\varphi}{\chi}}(\underline{k};\eta)=\frac{1}{2}\left(1\mp\cos\left(\eta(1-\eta)\frac{l_F^2k^2}{2\pi}\right)\right) \tag{2}$$

with $l_F=\sqrt{\lambda L}$ the Fresnel length. The time dependence in equation (1) is assumed to arise from advection of frozen refractive index structure through the propagation path at a mean velocity $\underline{v}$, which can vary along the path.

The linear array used in the AMSE experiment spans spatial lags in the horizontal direction (x coordinate) perpendicular to the propagation path. As the mean fluid motion, also in this direction, transports refractive index structure through the acoustic beam, the resulting acoustic fluctuations sweep across the array with an apparent speed determined by the proximity of the structure to the projector. Motion of refractive index structure near the projector causes acoustic fluctuations to sweep across the array with large apparent speed, while the speed of structure near the array is amplified only slightly when projected onto the array. This observation, a simple consequence of Taylor's hypothesis and spherical propagation geometry, implies a method for filtering the acoustic data to focus on refractive index structure at a particular point along the propagation path. The method is a variation of a space-time filtering technique originally developed for atmospheric sounding (Clifford and Churnside,1987).

To apply the filter, the acoustic time series at each receiver is shifted by a position-dependent delay before correlation:

$$\chi(t,x_j)\rightarrow\chi'(t,x_j)=\chi(t+\frac{x_j}{\mathrm{v}},x_j) \tag{3}$$

where x_j denotes the position of the jth receiver and v is the filter velocity. This operation aligns the time series at the different receivers so that fluctuations moving across the array with apparent speed v appear to be simultaneous. The model expression for the space-time correlation of the shifted acoustic signals is then

$$B_{\underset{\varphi}{\chi}}(\Delta x_{ij},\Delta t)\approx 2\pi k_i^2 L\int_0^1 d\eta\int d^2k e^{ik_x\Delta x_{ij}\left(\eta-\frac{\mathrm{v}_x(\eta)}{\mathrm{v}}\right)-ik_x\cdot\mathrm{v}_x(\eta)\Delta t}H_{\underset{\varphi}{\chi}}(\underline{k};\eta)F_n(\underline{k};\eta) \tag{4}$$

where $\Delta x_{ij}=x_i-x_j$. Fourier transforming in the time lag and forming a weighted sum over spatial lags gives the filtered spectrum

$$S_{\underset{\varphi}{\chi}}(\omega)=2\pi k_i^2 L\int_0^1 d\eta\int d^2k 2\pi\delta(\omega-k_x\,\mathrm{v}_x)g\left(k_x\left(\eta-\frac{\mathrm{v}_x(\eta)}{\mathrm{v}}\right)\right)H_{\underset{\varphi}{\chi}}(\underline{k};\eta)F_n(\underline{k};\eta) \tag{5}$$

where the spatial filter response function is

$$g(k)=\sum_{\Delta x\in S_F}w_{\Delta x}e^{ik\Delta x}\,. \tag{6}$$

Here S_F is the set of spatial lags spanned by the array (frequently called the sampling function) and $w_{\Delta x}$ is a filter weight associated with lag Δx. If a sufficiently dense set of spatial lags are represented in the array, the weights can be chosen to give a spatial filter response g which is strongly peaked around zero. Provided k_x is not too small, such a filter will select the region

$$\eta \approx \frac{v_x(\eta)}{v} \tag{7}$$

in the integral in equation (5). Since v is a parameter, the filter can be tuned to select any point along the propagation path.

With a single projector it is not possible to determine η independently of $v_x(\eta)$. However, use of additional information about v_x (e.g. direct measurements or a boundary layer mean flow model) permits model-based reconstruction of sound speed structure along the propagation path.

Implementation

Figure 5 shows the spatial lags spanned by the AMSE array with associated redundancies (number of distinct hydrophone pairs at each lag). Observations collected at redundant baselines are averaged together to reduce noise.

To apply the filter it is necessary to specify a set of weighting coefficients. A default choice of uniform weighting results in a filter response with large sidelobes, complicating interpretation of the filtered data. Figure 6a shows that, for the AMSE sampling function, the sidelobes levels resulting from uniform weighting exceed 25%.

To reduce sidelobe levels, optimized weights were computed using an iterative method based on minimizing the sum of squared differences between achieved sidelobe levels and a specified response pattern. Starting with uniform weights, we used a gradient-descent approach to minimize the sum-squared-error determined at the sidelobe positions. This algorithm is a minor modification of one published by Wu and Zielinski (Wu and Zielinski, 1993), which failed to converge for the sparse AMSE array. Figure 6b shows optimized filter responses determined with this approach in which sidelobe levels are below 10%, an acceptable level for this application.

When all the lags spanned by an array are integral multiples of the shortest lag, as in the AMSE array, the response function has secondary maxima called grating lobes. If grating lobes act upon input data the interpretation of filter output becomes ambiguous. In the design of sensor arrays, such effects are usually minimized either by adjusting array element separation or by tailoring the response of individual array elements. Neither alternative is available *post facto* for the AMSE array, so it is important to determine the possible impact of grating lobes on the spatial filter performance. Denoting the shortest lag by Δr (=0.5m), the first grating lobes are at wavenumbers $k_{gr}=\pm 2\pi/\Delta r$. The effective wavenumber of the shifted data is

$$|k| = \left| \frac{\omega}{v_x} \left(\eta - \frac{v_x}{v} \right) \right|. \tag{8}$$

Since $0<\eta$, $v_x/v<1$, the condition $|k|<|k_{gr}|$ that the filter input does not overlap the grating lobes holds if

$$|v_x| > \frac{\omega \Delta r}{2\pi}. \tag{9}$$

The 0.5 Hz sampling rate for acoustic data corresponds to a maximum (Nyquist) frequency of 0.25 Hz, implying that grating lobes do not affect the filter output if the mean current exceeds 12.5 cm/s everywhere along the acoustic path. For lower frequencies the requirement on minimum current speed is reduced proportionally. Since measured v_x at the current meter on the acoustic array was typically 10 cm/s or higher, grating lobe response is only expected to affect spatial filter output for the highest measured fluctuation frequencies.

Another implementation concern is performance of the spatial filter at low frequencies. When ω/v_x is comparable to the filter resolution Δk, the filter has little resolving power in η. However, the maximum effective wavenumber is also reduced and response from sidelobes at larger wavenumbers is no longer an issue. The filter weight optimization can be changed to minimize only those sidelobes within a limited wavenumber domain. This allows maintenance of a narrower central lobe (and thus better path-position resolution) as shown in figure 6b. In order to improve path resolution at low frequencies, we apply the filter weights corresponding to the solid curve in figure 6b at frequencies

$$\omega < 0.25\pi \frac{v_x}{\Delta r} . \qquad (10)$$

Using the resultant filter weights, application of the filter to the acoustic data proceeds in four steps:

- data are windowed and Fourier transformed
- a normalized cross-spectrum is constructed for each lag
- cross-spectra are multiplied by complex phasors which reflect the lag-dependent time delays of equation (3)
- cross-spectra are summed with appropriate filter weights to form the filtered spectrum.

5. Analysis and Results

Much of the AMSE data was collected during conditions of strongly stable stratification. Under such conditions the 3D spectra of temperature and conductivity fluctuations become anisotropic, and the 1D spectra deviate from the -5/3 power law behavior derived by Obukov and Corrsin for isotropic turbulence (Moseley and Del Balzo, 1976; Monin and Ozmidov, 1985). These characteristics may be accommodated in a simple model by generalizing the isotropic form to

$$F_n(\underline{k}, k_z) = C_n^2(\eta)(\underline{k}^2 + \alpha^2 k_z^2)^{-a} , \qquad (11)$$

where $\underline{k}$ is horizontal wavenumber, k_z is vertical wavenumber, α is an anisotropy parameter, and a=11/6 for turbulence. A similar spectral form has been used to model fine structure (Duda, et al., 1988). In general, the parameters C_n^2, α, and a will all depend on altitude in a vertically inhomogeneous environment, although we display this dependence explicitly only for C_n^2. The case $\alpha<1$ corresponds to refractive index structure with vertical correlation decaying more rapidly than horizontal correlation, consistent with stable stratification. If the structure is frozen and advected past a point sensor with a

known speed, the model parameters C_n^2/α and a may be fixed by fitting the 1-dimensional spectrum derived from equation (11) to the temporal spectrum of the data.

Substituting the refractive index spectral model into equation (5) for the filtered acoustic spectrum yields

$$S_{\underset{\varphi}{\chi}}(\omega) = (2\pi)^2 k_i^2 L \frac{C_n^2(\eta)}{\alpha} \frac{1}{\omega \Delta r} \frac{1}{2} \left(\frac{\omega^2}{v_x^2(\eta)} \right)^{\frac{1}{2}-a} \times \Gamma\left(\frac{1}{2}\right) \left(\frac{\Gamma\left(a-\frac{1}{2}\right)}{\Gamma(a)} \mp \mathrm{Re}\left(e^{i\bar{\omega}^2} \, U\left(\frac{1}{2}, \frac{3}{2}-a, -i\frac{\bar{\omega}^2}{\alpha^2}\right)\right)\right) \tag{12}$$

where U is the confluent hypergeometric function, Γ is the gamma function, and $\bar{\omega}^2 = \omega^2 / \omega_T^2$, with

$$\omega_T = \frac{v_x(\eta)}{l_F} \sqrt{\frac{2\pi}{\eta(1-\eta)}}. \tag{13}$$

Here quantities depending on η are evaluated at the value selected by the spatial filter. For AMSE, there is one value of η at which $v_x(\eta)$ is known, namely the path position corresponding to the altitude of the current meter. Comparison of measured acoustic spectra with predicted spectra provides a useful check on the validity of the several physical and modeling assumptions made in deriving equation (12).

Because of the stratified environment, only at times of strong mean current (>30 cm/s) does the AMSE environmental data show clear evidence of a turbulent regime. These cases are good tests of the spatial filtering approach, since several essential assumptions (frozen refractive index structure, horizontal homogeneity and horizontal isotropy) should be satisfied. Figure 7 shows environmental spectra from run 16. All spectra displayed here are normalized so that the integral over frequency equals 2π times the quantity variance. Note that sound refractive index spectra derived from measurements at CT1, CT2, and CT3 (the three lowest conductivity-temperature sensors) show a -5/3 power falloff indicative of turbulence.

Figure 8 shows the model filtered acoustic log-amplitude spectrum (using v_x and C_n^2/α derived from the CT2 environmental data) compared with data-derived log-amplitude spectra for runs 15 and 16. Both runs were at 100 kHz frequency. A good fit to the data is obtained with an anisotropy value $\alpha \approx 0.5$, down to frequencies where the spatial filter loses resolution.

It is interesting to compare the modeled and measured acoustic spectra in a non-turbulent case. Figure 9 shows temperature and salinity time series from CT2 for run 29. Both time series show large, intermittent steps indicative of transitions between a few discrete values. Another view of this data is shown in the T-S scatterplot displayed in figure 10, in which three or four clusters of points lie along a line of constant density ratio. One

structure which is consistent with this data is a stack of three or more layers of different water types, with each layer well mixed and with sharp boundaries between layers. Horizontal variation in layer thickness or altitude, when advected past the sensor by the mean current, would give signal time variation of the type observed. The time series from CT1 and CT3, above and below CT2, do not show similar strong variation in this run.

The refractive index spectra for run 29 environmental data are given in figure 11. The spectrum for CT2 has a slope of -2.6 over the spatial scales contributing most to acoustic amplitude fluctuations. Model predictions for filtered log-amplitude spectra are compared with the data from runs 28 and 29 (253 kHz) in figure 12. Again, agreement with the overall level of the data is excellent, and the model spectral form seems to capture the refractive index structure adequately for the acoustic scattering calculation.

As a final example, figure 13 shows the refractive index spectrum for run 38. This spectrum has a slope of -2 over the relevant spatial scales. Figure 14 shows the modeled acoustic log-amplitude spectrum compared with data for runs 37 and 38, with a good fit for α in the range 0.3-0.5. For these runs good acoustic phase data were available, and figure 15 shows the modeled filtered phase spectrum compared with data. Although the phase spectrum has only a weak dependence on the anisotropy parameter, the dependence on the power law decay of the refractive index spectrum is more apparent than for the log-amplitude spectrum. Figure 15 indicates that acoustic phase spectra are consistent with a refractive index spectrum with a decay exponent slightly below the -2 value measured in the environmental data.

Several of the acoustic runs (including runs 28-29) show frequent, strong fades in amplitude and produce variances $\langle\chi^2\rangle$ in the range 0.2-0.5 associated with the onset of saturation. Since the Rytov or weak scattering formalism implicit in the analysis above is not valid in the saturated regime, it is important to check this subset of data more carefully for other indications of saturation. One standard test is to look at the statistics of amplitude or intensity (Flatte, 1979): for weak or unsaturated scattering the log-amplitude and phase follow Gaussian statistics, while for saturated scattering the amplitude follows Rayleigh statistics. Figure 16 shows log-amplitude pdfs derived from several of the AMSE runs. Pdfs for runs 16 and 37 (both 100 kHz) are consistent with Gaussian statistics. The pdf for run 28 (253 kHz) exhibits larger variance but still has close to Gaussian shape. On the strength of this diagnostic the weak scattering analysis applied in the above discussion is probably valid. For comparison, the figure also shows pdfs for runs 31 and 42 (both 180 kHz); these distributions are clearly not Gaussian. Other diagnostics for saturation (intensity statistics, complex phasor plots) applied to these runs show evidence that they are in the partially saturated regime, with statistics determined by correlated micro-multipath.

6. Conclusions

Although the observed level of agreement between spatially filtered acoustic spectra and modeled acoustic spectra based on CT measurements is highly encouraging, this analysis is clearly an incomplete test of the spatial synthetic aperture filtering concept. The AMSE was an engineering feasibility experiment for SAS, and as such was not really designed or instrumented to demonstrate acoustic sounding of medium properties. A more definitive experiment (for similar BBL environments) would include the following improvements over the AMSE:

- denser vertical sampling of environmental measurements (including current velocity), with measurement stations located closer to the middle of the acoustic path,
- a more rapid acoustic sampling rate than the 0.5 Hz used in AMSE, to better delineate the "knee" frequency ω_T in the acoustic log-amplitude spectrum,
- multiple projectors deployed parallel to the receiver array and used to determine flow velocity independently from refractive index structure.

As an example of how multiple projectors might be used to determine flow velocity, consider an experiment with two projectors at positions x_1^T and x_2^T, with $\Delta x^T = x_1^T - x_2^T$. Construct sum and difference acoustic signals for each receiver, e.g.

$$\chi_{i+}(t) = \chi_{i1}(t) + \chi_{i2}(t) \quad \chi_{i-}(t) = \chi_{i1}(t) - \chi_{i2}(t) \tag{14}$$

where χ_{i1} denotes the log-amplitude signal at receiver i from projector 1, etc. Then, under Taylor's hypothesis and the assumption of weak scattering, the covariances of the sum and difference signals are

$$< \chi_{i\pm}(t+\Delta t)\chi_{j\pm}(t) > \approx$$
$$2\pi k_i^2 L \int_0^1 d\eta \int d^2k e^{ik_x \Delta x_{ij} - ik_x v_x \Delta t} 4 \begin{Bmatrix} \cos^2\left(k_x \Delta x^T (1-\eta)/2\right) \\ \sin^2\left(k_x \Delta x^T (1-\eta)/2\right) \end{Bmatrix} H_\chi(\underline{k};\eta) F_n(\underline{k};\eta) \tag{15}$$

and the filtering procedure previously described yields spectra

$$S_{\chi\pm}(\omega) \approx$$
$$2\pi k_i^2 L \int_0^1 d\eta \int d^2k 2\pi\delta(\omega - k_x v_x) g\left(k_x\left(\eta - \frac{v_x}{v}\right)\right) 4 \begin{Bmatrix} \cos^2\left(k_x \Delta x^T (1-\eta)/2\right) \\ \sin^2\left(k_x \Delta x^T (1-\eta)/2\right) \end{Bmatrix} H_\chi(\underline{k};\eta) F_n(\underline{k};\eta). \tag{16}$$

Upon forming the ratio we find

$$S_{\chi-}(\omega) / S_{\chi+}(\omega) \approx \tan^2\left(\frac{\omega \Delta x^T}{2}\left(\frac{1}{v_x} - \frac{1}{v}\right)\right) \tag{17}$$

which may be solved uniquely for v_x provided that $\omega \Delta x^T$ is not too large. To reduce inaccuracies caused by noisy spectral estimates, equation (17) would be integrated over an appropriate frequency window in practice. An alternative scheme for sounding velocity and refractive index structure separately, using multiple projectors and receivers, may be found in the reference by Farmer and Crawford.

Since research SAS systems operating at frequencies of 50 kHz and above are now coming into operation, we briefly mention the possibility of using a SAS to characterize BBL (or other) medium structure. This could be done by seeding a smooth bottom with calibrated targets (spheres or corner reflectors). The SAS would be focused down to an azimuth resolution on the order of the mean separation between targets; additional system capability for azimuth resolution would be traded off in favor of tracking time histories of acoustic returns from targets moving through the SAS field of view. To derive medium properties, resulting data would be spatially filtered using model-based algorithms similar to those discussed above. An important benefit of applying spatial filtering to data from a 2D field of targets (in a horizontally homogeneous medium) is the opportunity for additional averaging to reduce errors in derived medium properties.

Acknowledgements

This work was supported by the Office of Naval Research, Physical Oceanography Program. The author wishes to thank Bob Gran and Randy Patton of DTI for useful technical conversations and help with the data analysis.

References

J.T. Christoff, C.D. Loggins, and E. L. Pipkin, "Measurement of the temporal phase stability of the medium," JASA **71**, 1606, 1982.

S. F. Clifford and J. H. Churnside, "Refractive Turbulence Profiling Using Synthetic Aperture Spatial Filtering of Scintillation," App. Optics **26**, 1295, 1987.

G. B. Crawford, R. J. Lataitis, and S. F. Clifford, "Remote Sensing of Ocean Flows by Spatial Filtering of Acoustic Scintillations: Theory," JASA **88**, 442, 1990.

T. F. Duda, S. M Flatte, and D. B. Creamer, "Modelling Meter-Scale Acoustic Intesity Fluctuations From Oceanic Fine Structure and Microstucture," J. Geophys. Res. **93**, 5130, 1988.

D. B. Farmer and S. F. Clifford, "Space-Time Acoustic Scintillation Analysis: A New Technique for Probing Ocean Flows," IEEE Jour. Ocean. Eng. **OE-11**, 42, 1986.

D. M. Farmer, S. F. Clifford, and J. A. Verrall, "Scintillation Structure of a Turbulent Tidal Flow," J. Geophys. Res. **92**, 5369, 1987.

D. M. Farmer and G. B. Crawford, "Remote Sensing of Ocean Flows by Spatial Filtering of Acoustic Scintillations: Observations," J. Acoust. Soc. Am. **90**, 1582, 1991.

D. M. Farmer and D. DiIorio, "Two Dimensional Acoustical Propagation in a Stratified Shear Flow," Institute of Ocean Sciences preprint, 1992.

S. M. Flatte (Ed.), Sound Transmission through a Fluctuating Ocean, Cambridge U. Press, Cambridge, 1979.

V. M. Gorelov and S. V. Dotsenko, "Correlation Description of Two-dimensional Anisotropic Sound Fields," Sov. Phys. Acoust. **35**, 255, 1989.

P. T. Gough and M. P. Hayes, "Measurements of acoustic phase stability in Loch Linnhe, Scotland," JASA **86**, 837, 1989.

R. W. Lee and J. C. Harp, "Wave Scattering in Random Media, with Applications to Remote Probing," Proc. IEEE **57**, 375, 1969.

A. S. Monin and R. V. Ozmidov, Turbulence in the Ocean, D. Reidel Pub., Dordrecht, 1985.

W. B. Moseley and D. R. Del Balzo, "Horizontal Random Temperature Structure of the Ocean," J. Phys. Ocean. **6**, 267, 1976.

R. W. Schmitt Jr., "The Growth Rate of Supercritical Salt Fingers," Deep Sea Res. **26A**, 23, 1979.

A. J. Tardif (ed.), "Synthetic Aperture Sonar Medium Stability Experiment," Raytheon Company Submarine Signal Division Report R1325, 1973.

L. Wu and A. Zielinski (1993), "An Iterative Method for Array Pattern Synthesis," IEEE J. Ocean Engin. **18**, 280.

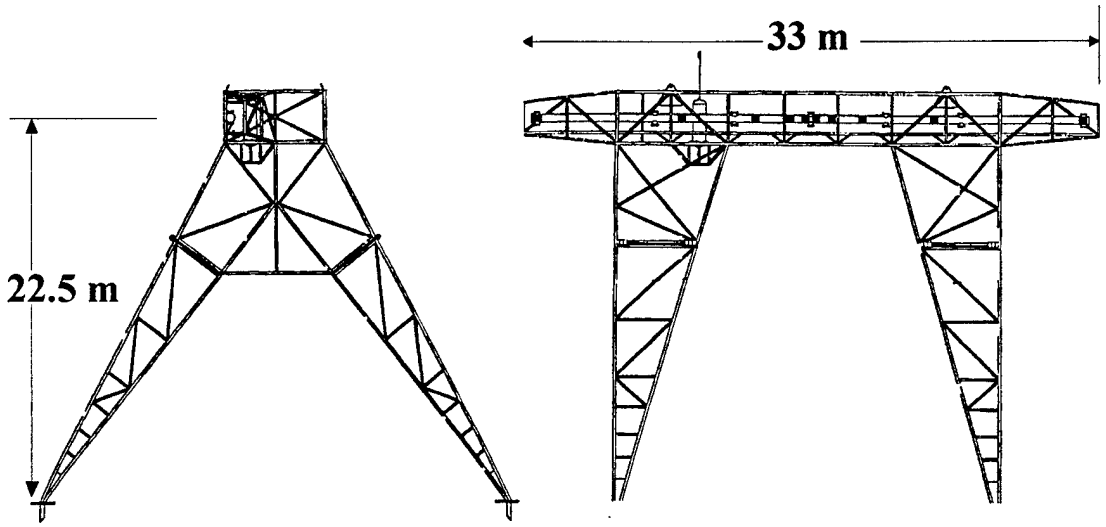

Figure 1. AMSE acoustic array support structure. Hydrophones are mounted along the pipe carried by the horizontal truss. CTD and current meter instruments are mounted to the outer corner of a vertical truss.

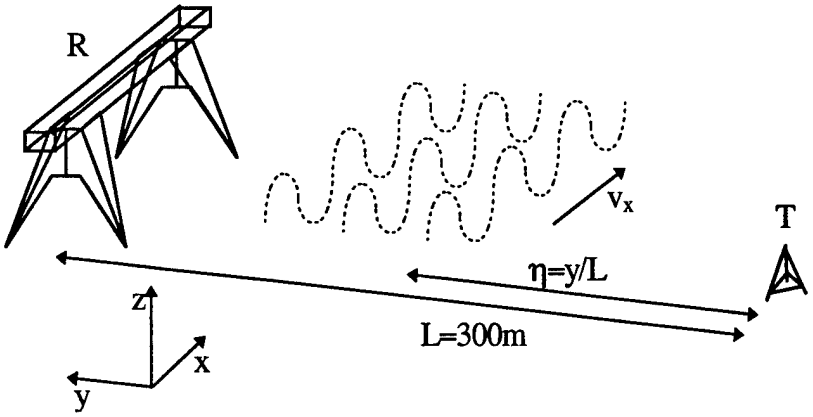

Figure 2. AMSE experiment geometry.

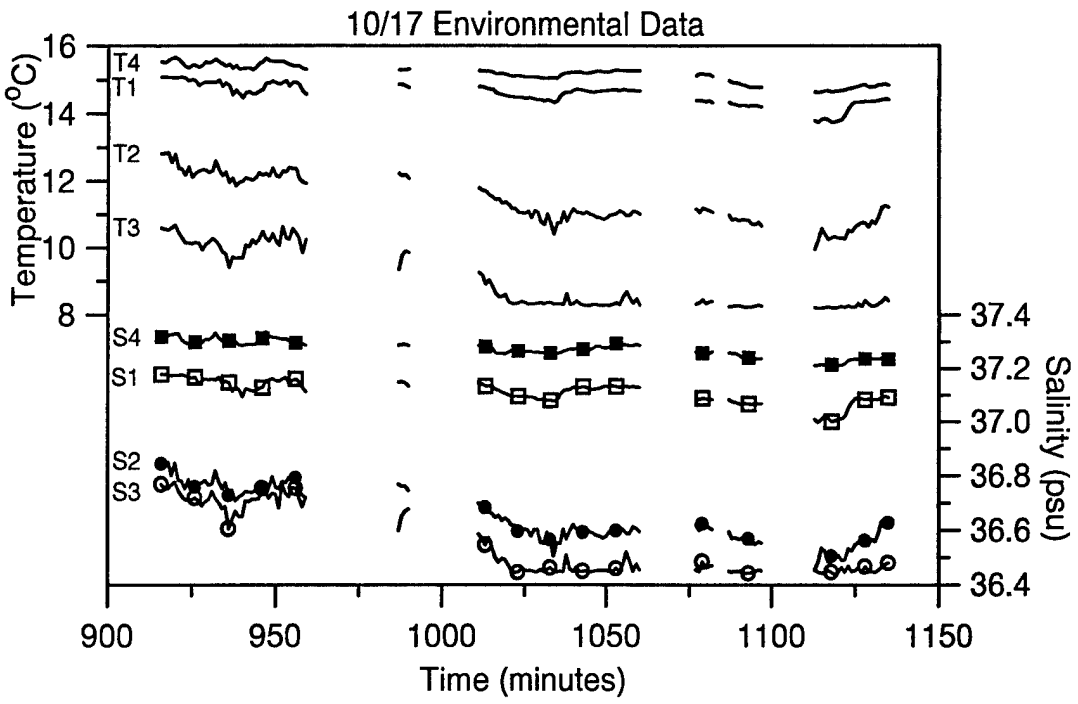

Figure 3a. Temperature and salinity data for 10/17 (1 minute average).

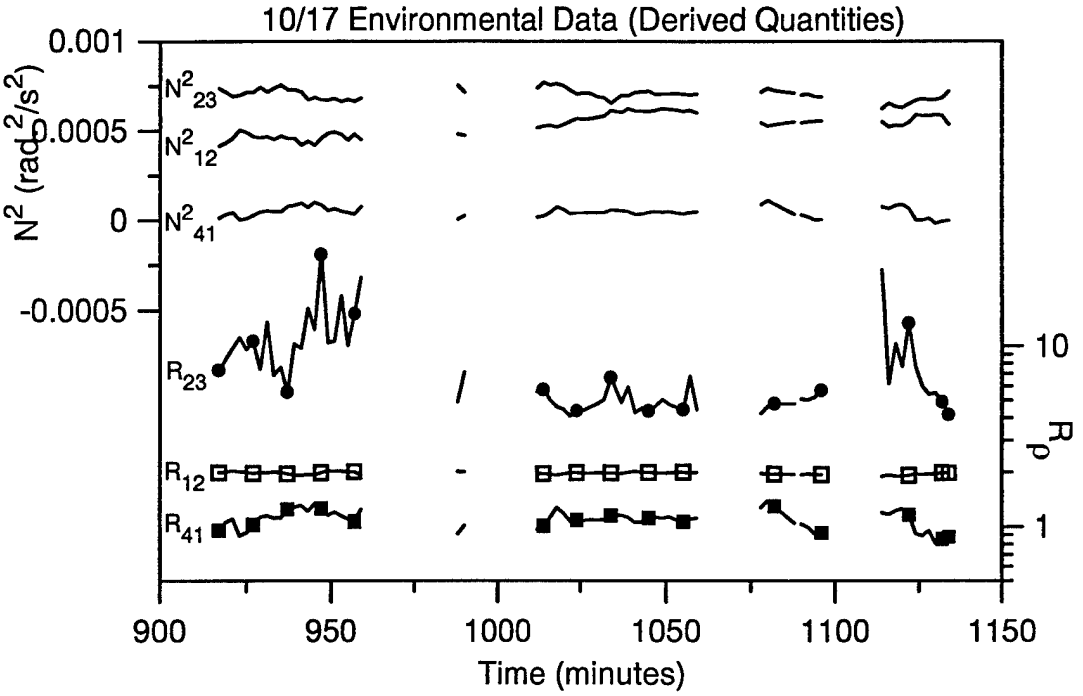

Figure 3b. Brunt-Vaisala frequency and density ratio for 10/17 (2 minute average).

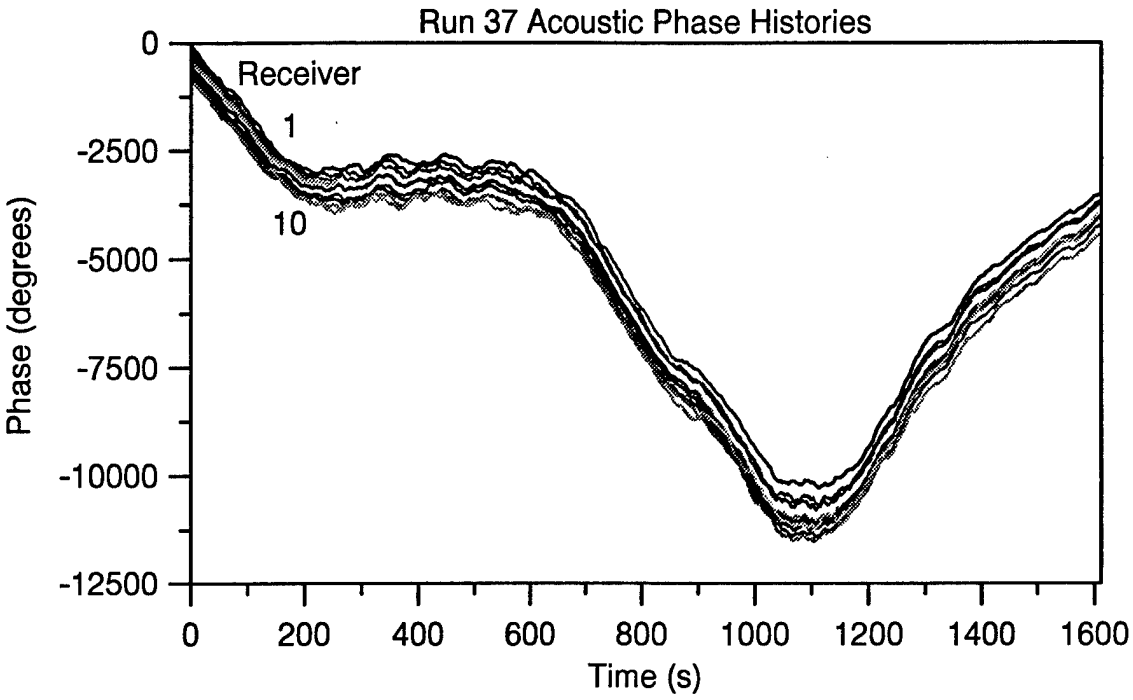

Figure 4a. Acoustic phase histories for run 37. Acoustic frequency is 100 kHz.

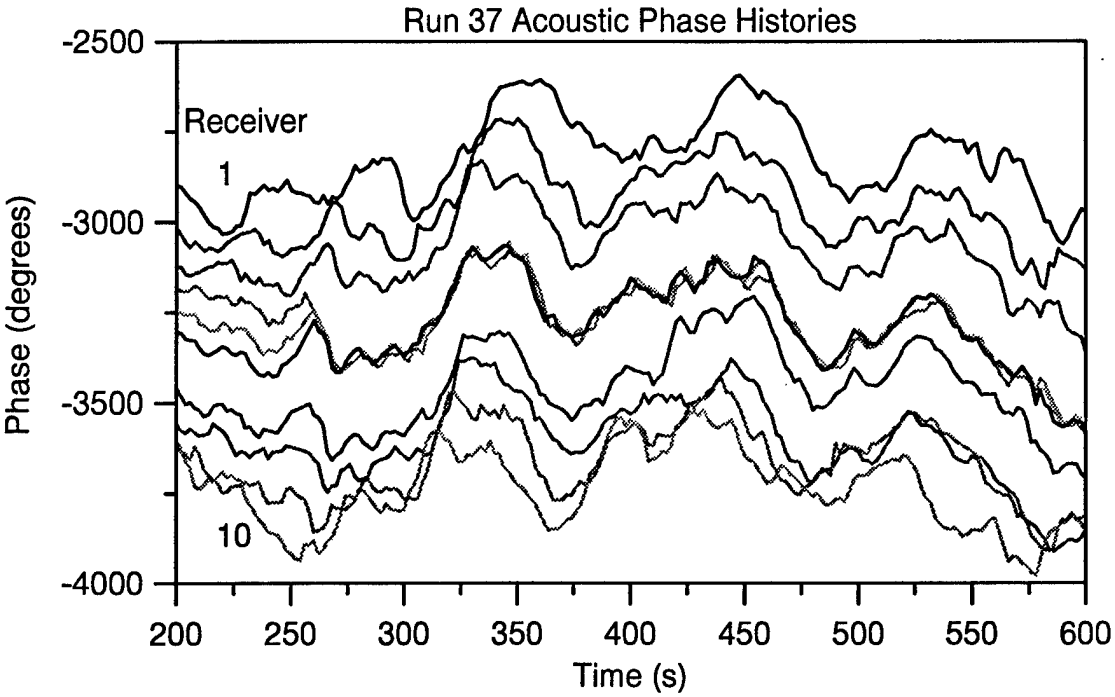

Figure 4b. Detail of run 37 phase histories (offset for display).

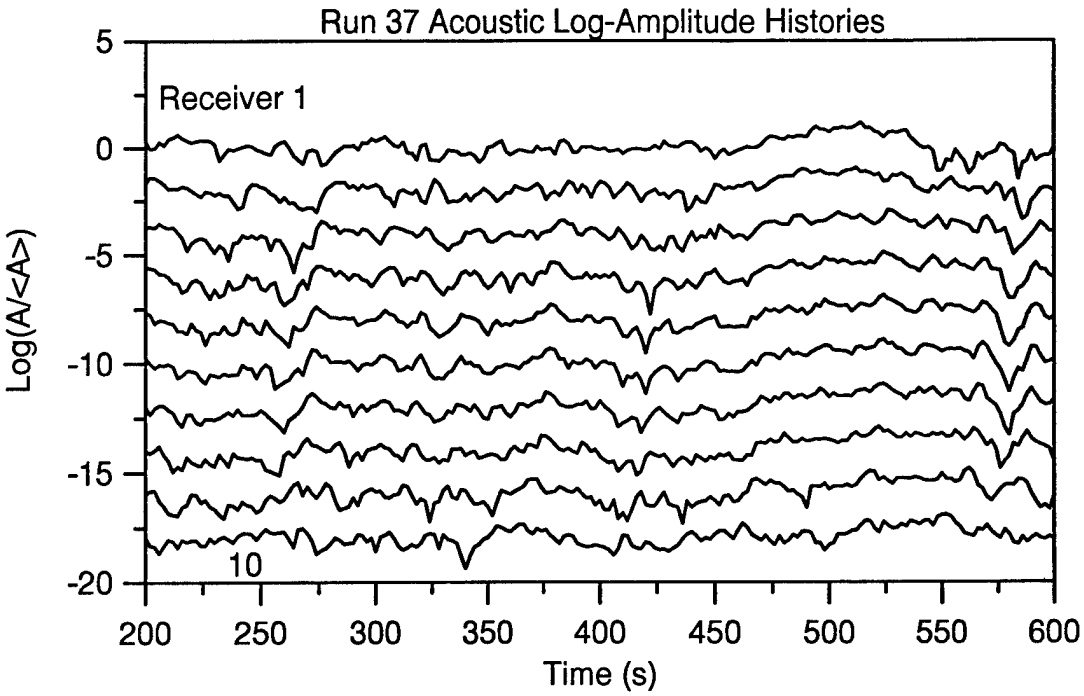

Figure 4c. Detail of run 37 log-amplitude histories (offset for display).

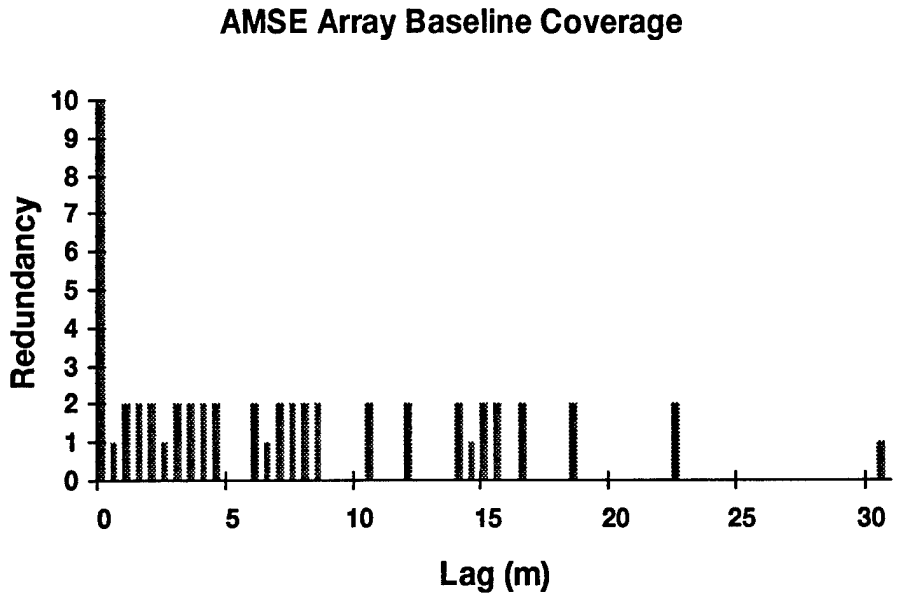

Figure 5. Spatial lags spanned by AMSE acoustic array.

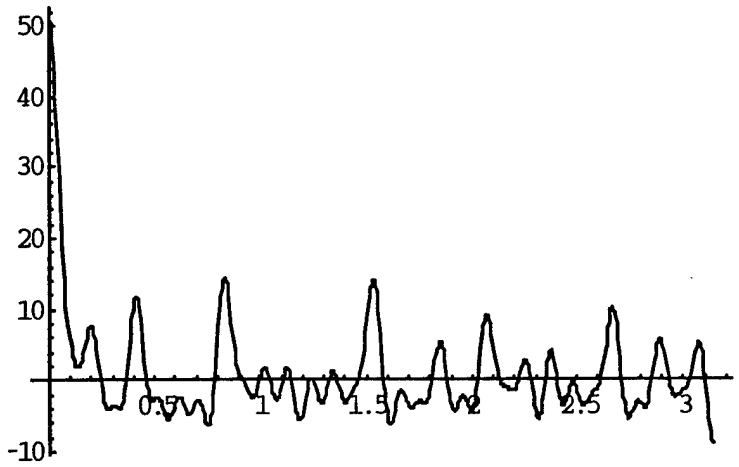

Figure 6a. Filter response g(kΔr) for uniform filter weights.

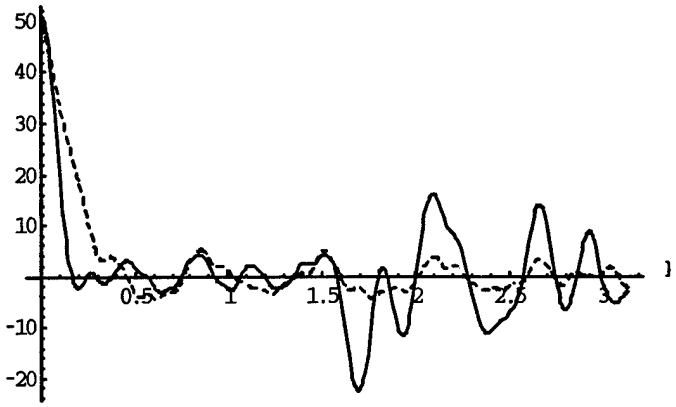

Figure 6b. Filter response g(kΔr) with optimized filter weights. Solid line—sidelobes minimized for $|k\Delta r|<\pi/2$. Dashed line—sidelobes minimized for $|k\Delta r|<2\pi$.

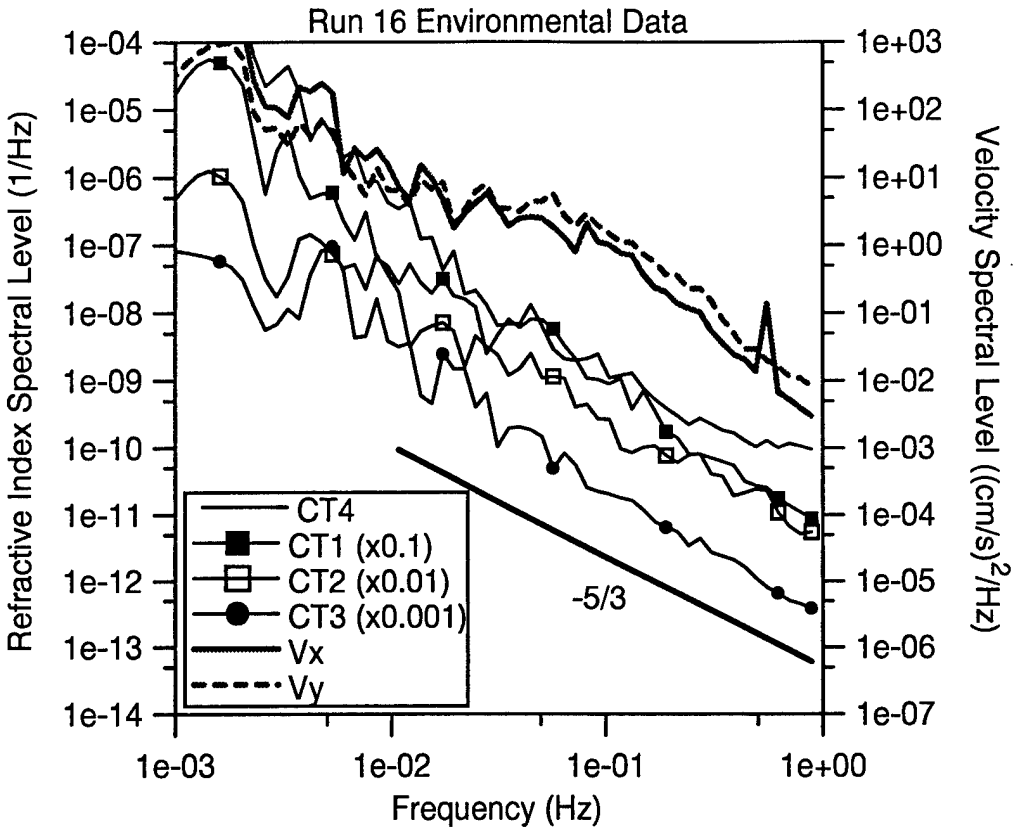

Figure 7. Refractive index and velocity spectra for run 16.

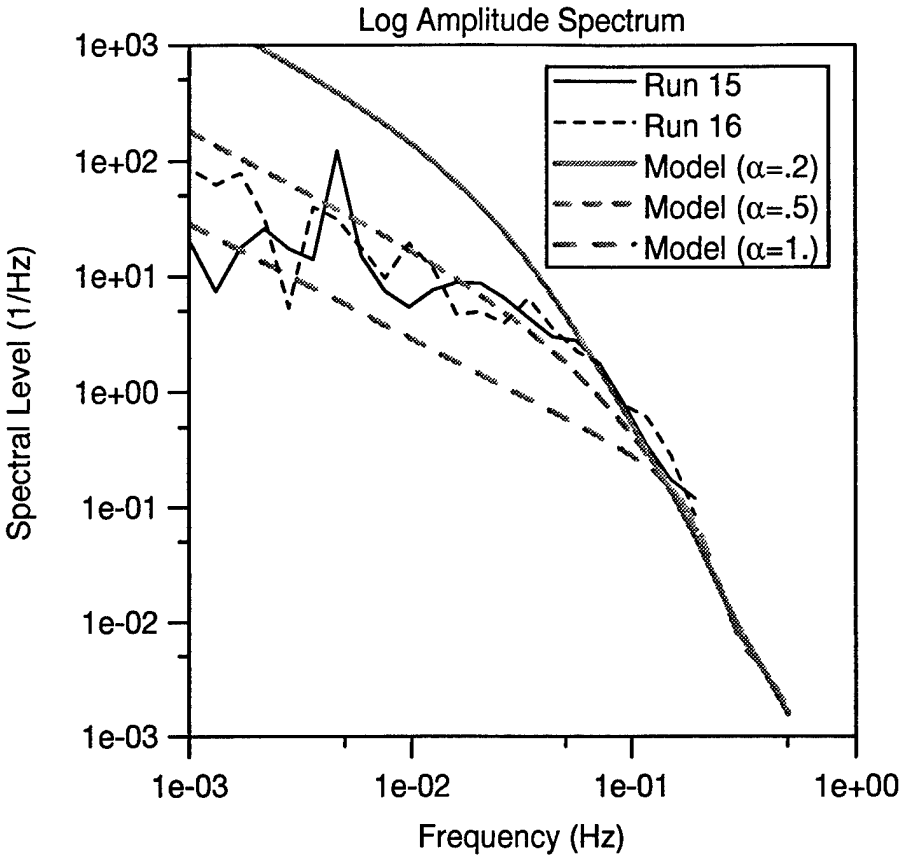

Figure 8. Comparison of filtered log-amplitude acoustic spectrum (runs 15 and 16) with model calculation using CT-derived spectra. Acoustic frequency is 100 kHz.

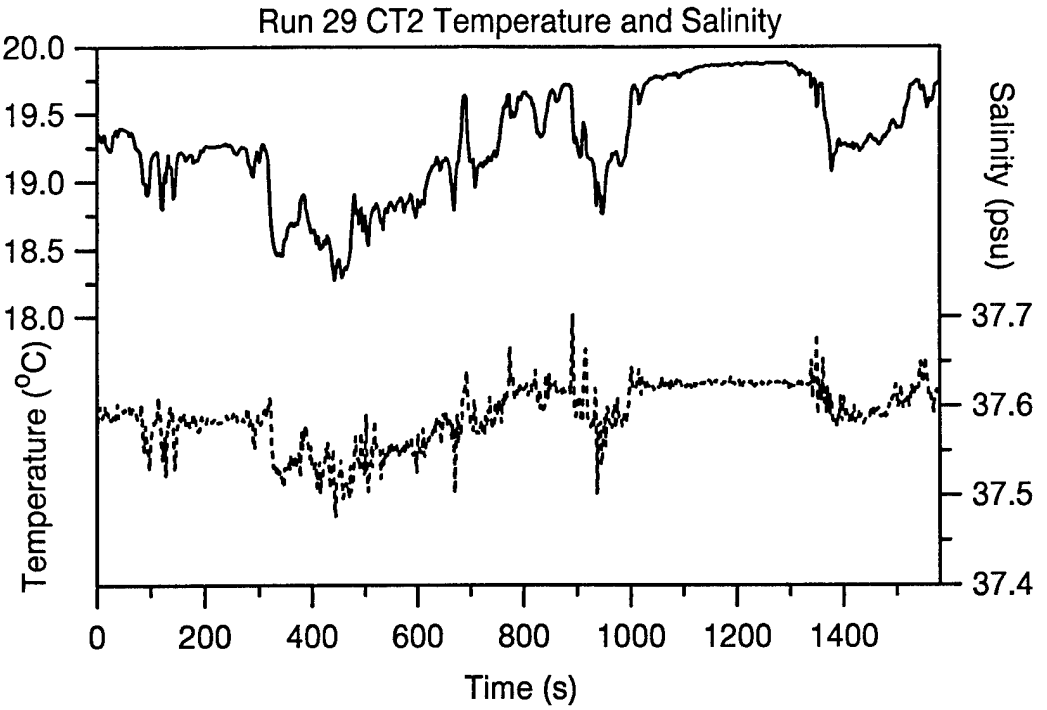

Figure 9. Run 29 CT2 temperature and salinity time series. Discrete steps in temperature and salinity may reflect advection of distorted mixed layers past the sensor.

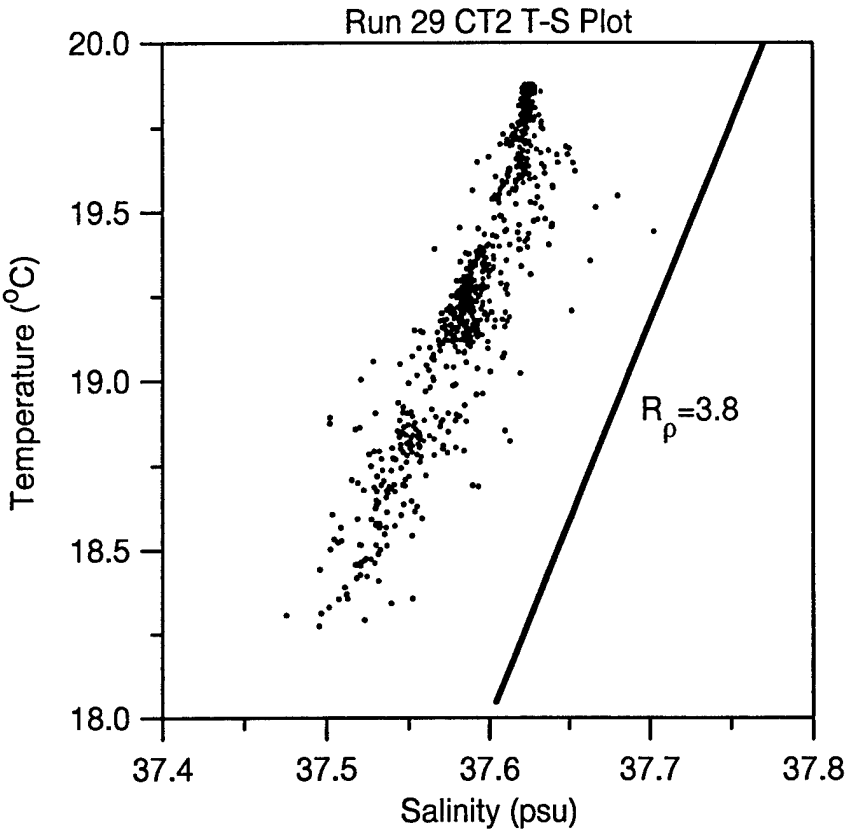

Figure 10. Run 29 CT2 T-S plot.

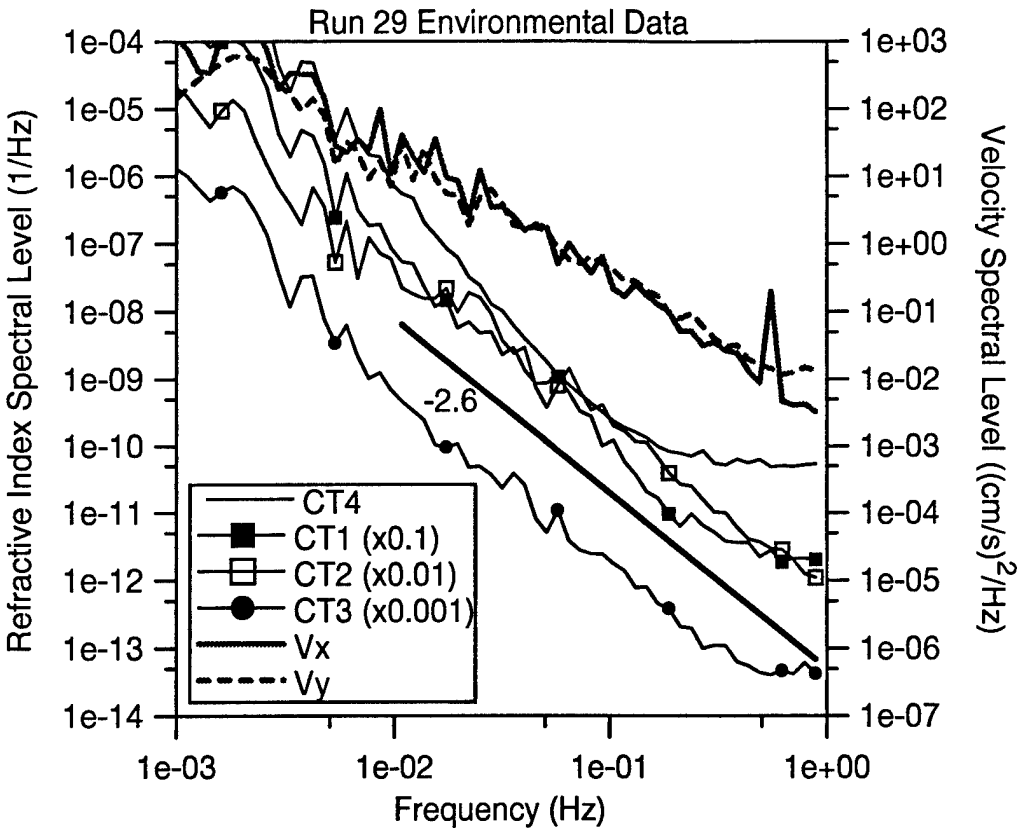

Figure 11. Refractive index and velocity spectra for run 29.

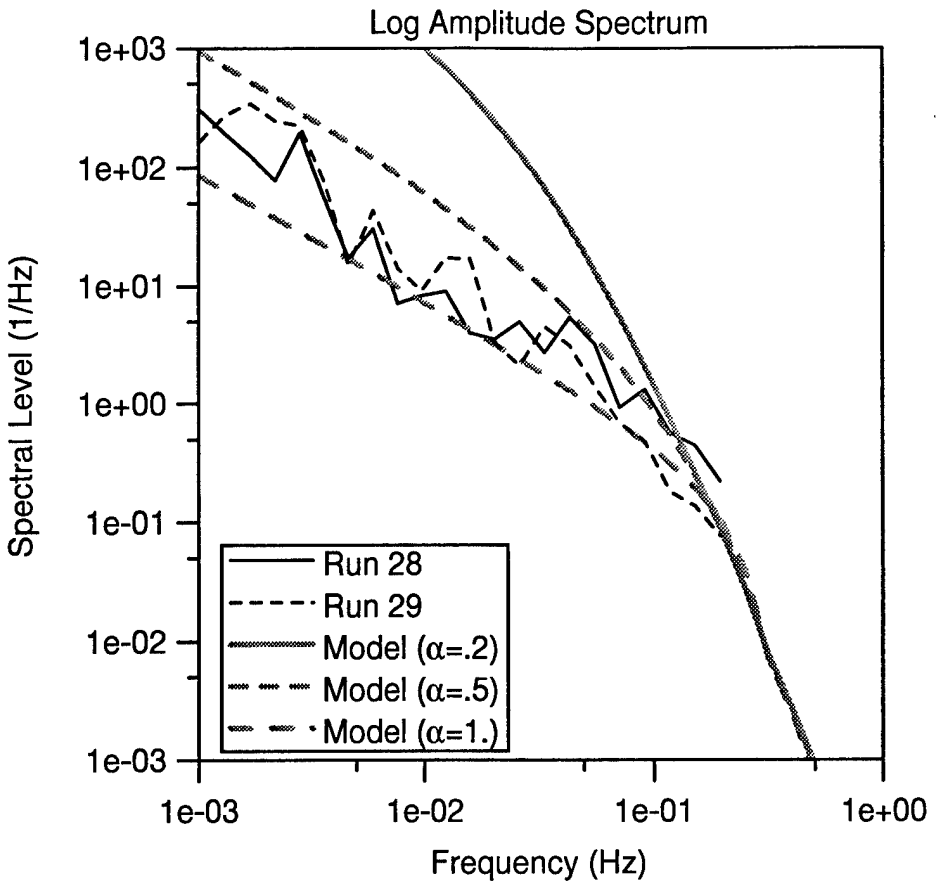

Figure 12. Comparison of filtered log-amplitude acoustic spectrum (runs 28 and 29) with model calculation using CT-derived spectra. Acoustic frequency is 253 kHz.

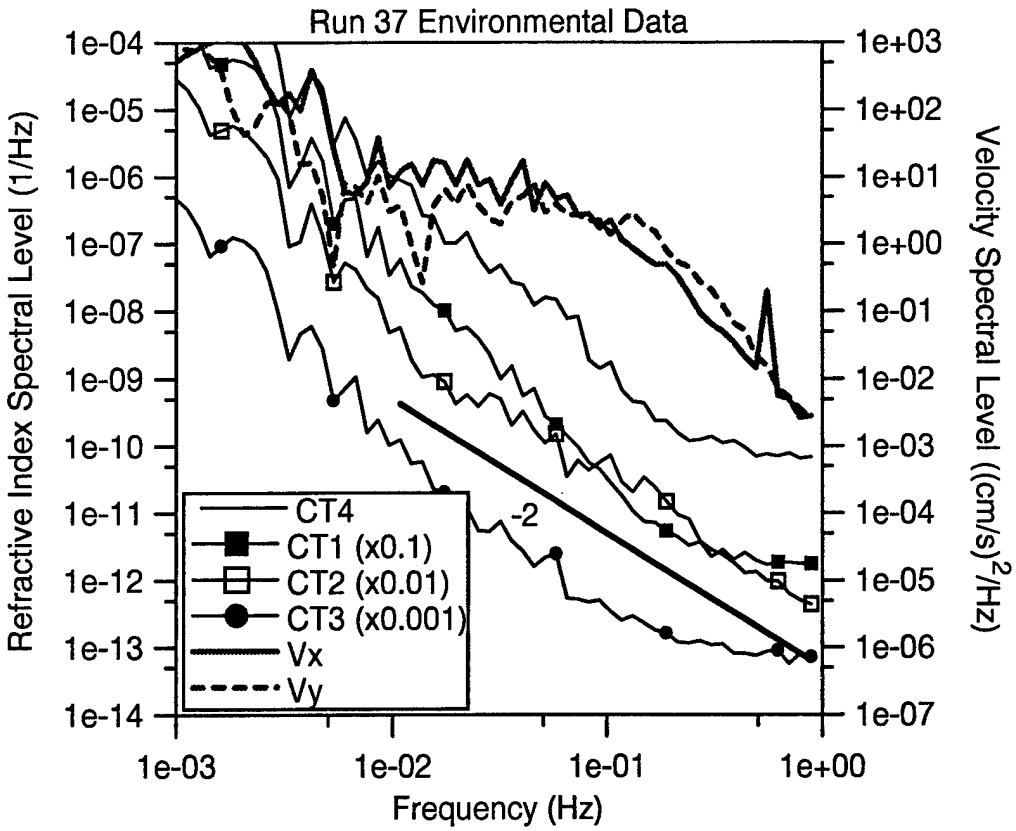

Figure 13. Refractive index and velocity spectra for run 37.

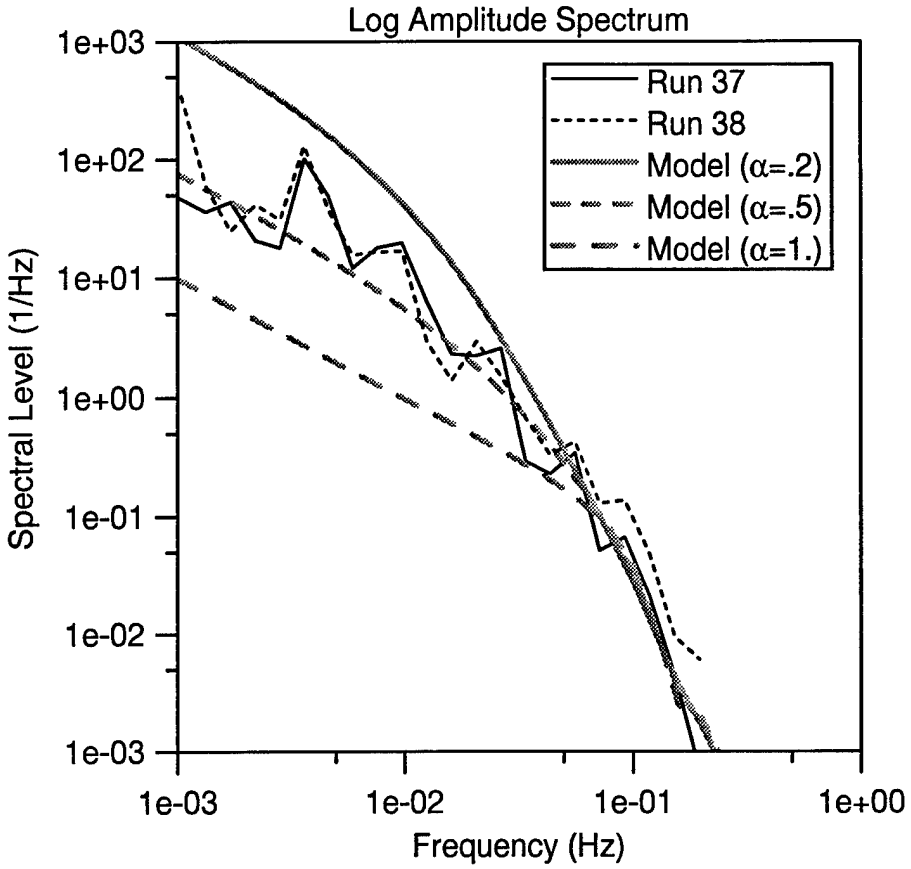

Figure 14. Comparison of filtered log-amplitude acoustic spectrum (runs 37 and 38) with model calculation using CT-derived spectra. Acoustic frequency is 100 kHz.

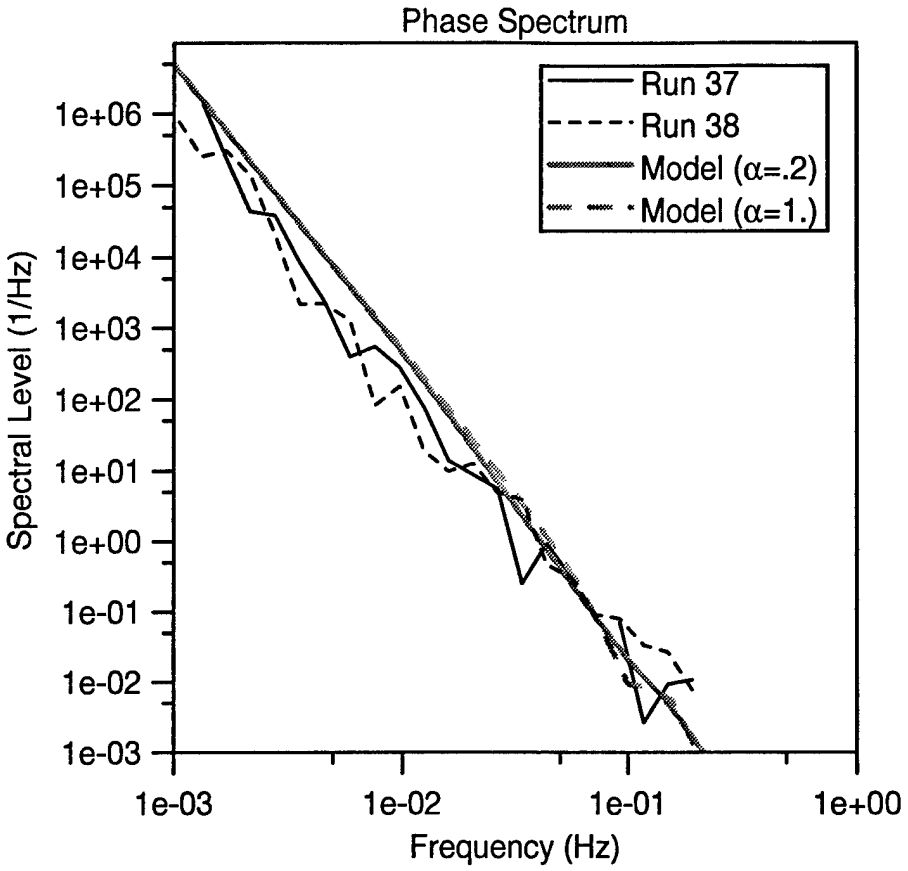

Figure 15. Comparison of filtered phase spectrum (runs 37 and 38) with model calculation.

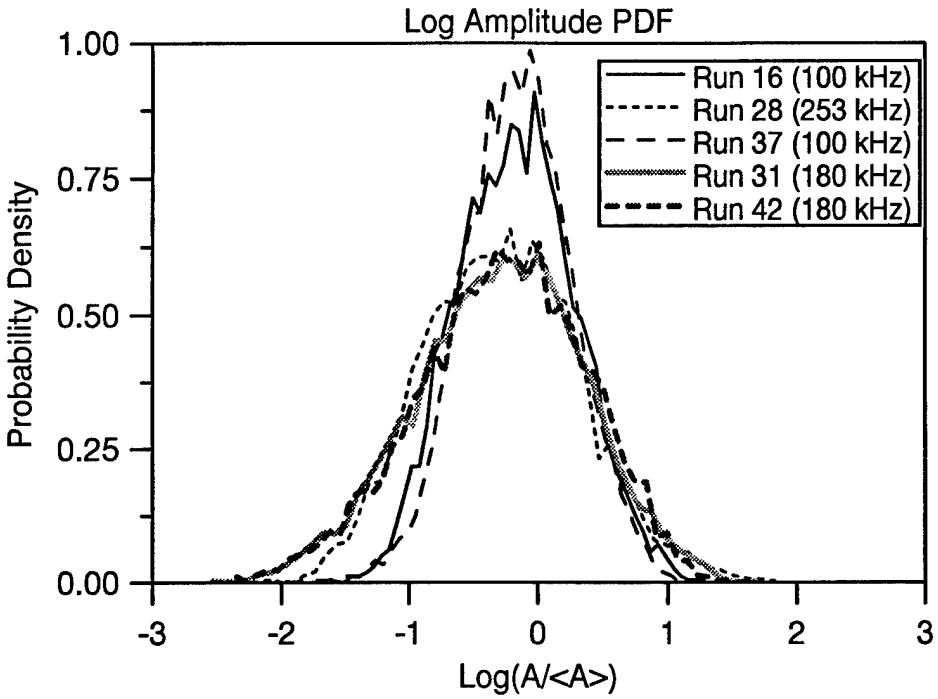

Figure 16. Probability density functions for log amplitude. Non-Gaussian pdfs indicate onset of strong scattering.